Available online at www.sciencedirect.com
SCIENCE DIRECT
Acta Materialia 54 (2006) 1297–1306
Acta MATERIALIA
www.actamat-journals.com

A sintering model for thermal barrier coatings

R.G. Hutchinson [a], N.A. Fleck [a,*], A.C.F. Cocks [b]

[a] Cambridge University Engineering Department, Trumpington Street, Cambridge CB2 1PZ, UK
[b] Department of Engineering, Leicester University, Leicester LE1 7RH, UK

Received 15 September 2005; received in revised form 23 October 2005; accepted 26 October 2005
Available online 18 January 2006

Abstract

A mathematical model is developed for the progressive sintering of ceramic columns in a thermal barrier coating made using the electron beam–physical vapour deposition route. The model assumes that inter-columnar sintering is driven by changes in the interface energy and elastic stored energy of the columns. The analysis reveals the sensitivity of the sintering rate to the in-plane elastic modulus as well as to an imposed thermal mismatch strain, interfacial energies and diffusivities. It is shown that mud-cracking of the coating leads to a drop in in-plane stress within the coating and thereby to accelerated sintering. Explicit calculations are reported for the evolution of sintering within an array of mud-cracked columns, and for the density of mud cracks.

Keywords: Thermal barrier coatings; Sintering; Fracture; Mud-cracking; Interface diffusion

1. Introduction

Turbine blades in the high-pressure, high-temperature stages of gas turbines are manufactured from creep-resistant nickel or cobalt alloys. The blades are internally air-cooled and are commonly thermally insulated by a ceramic–metallic multi-layer known as a thermal barrier coating (TBC). Two distinct architectures of ceramic coating are achievable: a roughly equiaxed microstructure of splats produced by air plasma spray and a columnar microstructure produced by electron beam–physical vapour deposition (EB-PVD) (e.g. see Ref. [1]). In this paper, we focus on the in-service sintering behaviour of TBCs made using the EB-PVD route.

Typically, EB-PVD coatings comprise a 100–200 μm thick layer of columnar yttria-stabilised zirconia (typically, 7YSZ) with an in-plane grain size of 5–10 μm, see Fig. 1. Thermal insulation against hot combustion gases is ensured by the low thermal conductivity of the YSZ layer, while oxidation resistance is achieved by an underlying thermally grown oxide (TGO) layer of alumina. The alumina sits upon an underlying aluminium-rich bond coat and it progressively thickens from about 2 μm after deposition to about 10 μm during service. The YSZ top layer is deposited at approximately 1300 K, and possesses a columnar structure by incoherent nucleation and selective growth upon the underlying TGO. Gaps of width 0.1–1 μm separate the columns and confer in-plane strain compliance to the coating: the coating can thereby accommodate thermal mismatch strains with the underlying superalloy substrate due to the thermal cycling.

During engine operation, the surface temperature of the TBC system may reach 1400 K, with the protected metallic substrate reaching a temperature of 1200 K. The temperature cycles between ambient temperature (300 K) and the maximum service temperature. Sintering of the top layer occurs rapidly at first over short length scales, and then more slowly over longer length scales. Initially, the feathery edges of the columns are rounded off by rapid local diffusion. Sintering at random contact points between the YSZ columns follows, and causes the isolated columns to have the macroscopic response of a layer with finite in-plane

* Corresponding author. Tel.: +44 1223 332662.
E-mail address: naf1@eng.cam.ac.uk (N.A. Fleck).

1359-6454/$30.00
doi:10.1016/j.actamat.2005.10.056

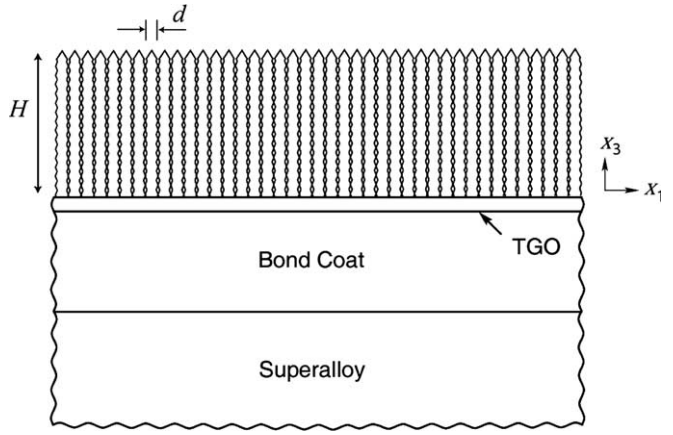

Fig. 1. A TBC system, with a thermally insulating top layer of columnar YSZ, a TGO layer of alumina, an aluminium-rich bond coat and an underlying substrate of creep-resistant superalloy.

stiffness and strength. Consequently, the strain compliance drops (e.g. see Refs. [2,3]). The inter-columnar sintering also allows erosion cracks to communicate from one column to the next at the sintered junctions, thereby reducing the erosion resistance of the coating (shown experimentally by Wellman and Nicholls [4]). The build-up of tensile stress within the top layer due to inter-columnar sintering can be sufficiently large to lead to mud-cracking upon cooling [5]. Mud-cracking relieves the in-plane tensile stress within the clusters, and thereby accelerates inter-columnar sintering within each cluster.

In this paper, the variational technique of Cocks et al. [6] is used to model the interfacial diffusion of matter at the local contacts between columns. As the columns sinter together, and the in-plane sintering strain evolves, overall strain compatibility with the substrate dictates the build-up of in-plane tensile stress. The increase in stored elastic strain energy within the TBC layer reduces the driving force for sintering and thereby reduces the sintering rate. The possibility of mud-cracking of the thermal barrier layer is also explored: the reduction of in-plane modulus due to mud-cracking reduces the degree of elastic constraint upon sintering and thereby increases the sintering rate of the columns within each cluster. The paper concludes with a discussion of the sensitivity of mud-cracking density to the degree of sintering.

2. Problem statement

We consider two problems in turn, A and B. *Problem A* involves the progressive sintering of an infinite TBC layer of columns upon a half-space, as shown schematically in Fig. 2(a). In *Problem B*, the progressive sintering of a set of columns occurs within a circular cylindrical cluster of radius R, as shown schematically in Fig. 2(b). In both problems, the TBC layer is of height H and is perfectly bonded to the substrate. The layer contains columns of square cross-section, of dimension d by d, aligned with the in-plane axes (x_1, x_2). The layer thickness is along the x_3 direction, with the origin located at the bottom of the columnar layer.

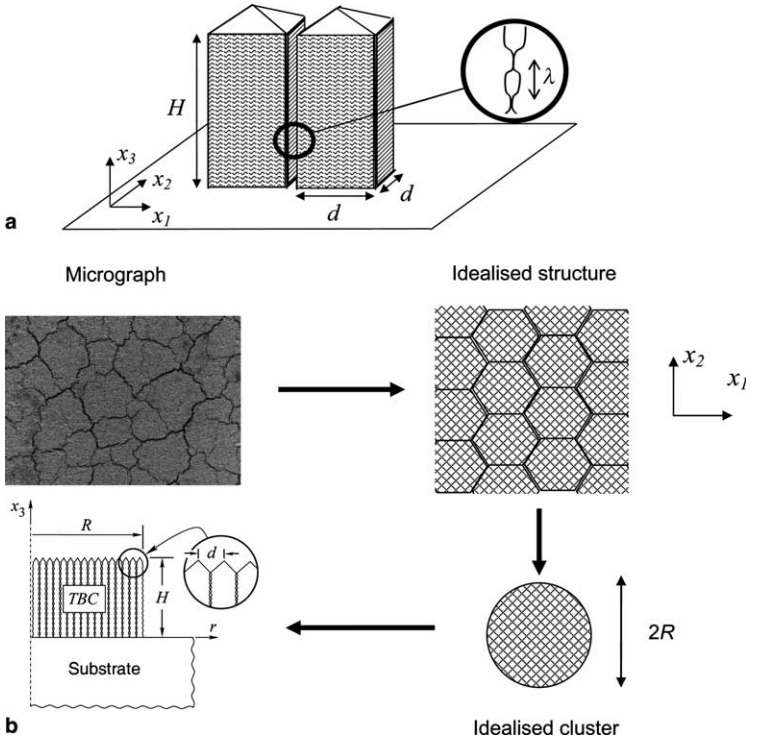

Fig. 2. (a) Sintering of neighbouring TBC columns, each of cross-section $d \times d$, upon a half-space. The local roughness at contacts is of wavelength λ. (b) The mud-cracked TBC layer is idealised by an assembly of circular clusters, each of height H and radius R. The clusters comprise columns which progressively sinter together, and are perfectly bonded to the substrate.

3. Problem A: inter-columnar sintering of a constrained, uncracked TBC layer

We impose an arbitrary temperature distribution within the uncracked columnar layer $T(x_3)$ which may be greater than or less than the deposition temperature T_D. The task is to determine the time evolution of inter-columnar sintering due to the imposed thermal mismatch associated with $T(x_3)$. The restraint of the substrate is included in the analysis.

3.1. Global considerations

The TBC layer can be treated as a continuum with an in-plane isotropic thermal expansion mismatch strain $\varepsilon^{T}_{\alpha\beta}(x_3) = \varepsilon^{T}(x_3)\delta_{\alpha\beta}$ relative to the underlying substrate, where α and β independently range over 1–2. Here, $\delta_{\alpha\beta}$ is the usual two-dimensional Kronecker delta symbol and the thermal expansion mismatch strain $\varepsilon^{T}(x_3)$ is

$$\varepsilon^{T} = \alpha_{TBC}(T(x_3) - T_D) - \alpha_S(T_S - T_D) \tag{1}$$

in terms of the coefficients of thermal expansion α_{TBC} and α_S of the columnar layer and substrate, respectively. Note that the deposition temperature T_D is taken as the reference temperature and defines the initial stress-free configuration. In formulating the sintering problem, the temperature field $T(x_3)$ can in principle vary with time, but in the numerical examples given we shall limit attention to the steady-state case, with a steady-state temperature profile across the film. The numerical solution at any position x_3 within the film depends only upon the time-independent local value of $\varepsilon^{T}(x_3)$, and solutions are obtained for selected values of ε^{T}.

As inter-columnar sintering proceeds, an equi-biaxial sintering strain $\varepsilon^{S}_{\alpha\beta}(x_3)$ evolves with time, where $\varepsilon^{S}_{\alpha\beta}(x_3) = \varepsilon^{S}(x_3)\delta_{\alpha\beta}$ can be expressed in terms of the scalar sintering strain ε^{S}. While $\varepsilon^{T}(x_3)$ can be positive or negative, sintering leads to an increasingly negative value for ε^{S}. A variational approach is employed below in order to calculate the time evolution of $\varepsilon^{S}(x_3)$ based upon an assumed contact geometry between neighbouring TBC columns (see Fig. 3). The substrate is taken to be much thicker than the TBC layer, such that the in-plane strain in the TBC layer relative to the substrate is zero. Consequently, the elastic strain within the TBC $\varepsilon^{E}_{\alpha\beta}(x_3)$ is given by

$$\varepsilon^{E}_{\alpha\beta}(x_3) = -(\varepsilon^{T}_{\alpha\beta}(x_3) + \varepsilon^{S}_{\alpha\beta}(x_3)). \tag{2}$$

The normal stress components $\sigma_{\alpha 3}$ and in-plane shear stress component σ_{12} vanish, while the in-plane direct stress components are

$$\sigma_{\alpha\beta} = \frac{E}{1-\nu}\varepsilon^{E}_{\alpha\beta} \tag{3}$$

in terms of the in-plane effective Young's modulus E and Poisson's ratio ν of the film. Consequently, the stored elastic strain energy per unit volume of TBC $U(x_3)$ is

$$U(x_3) = \frac{E}{1-\nu}(\varepsilon^{E}_{11})^2. \tag{4}$$

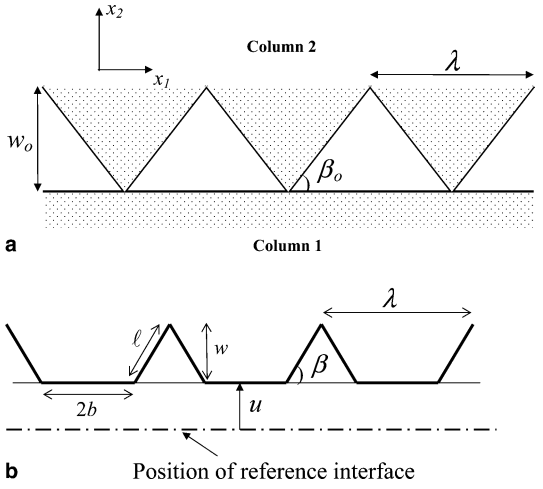

Fig. 3. Idealisation of surface roughness. (a) Reference configuration. (b) Current configuration, where column 1 has displaced an amount u with respect to column 2 from the reference configuration.

3.2. Local considerations

3.2.1. Contact geometry

It is envisaged that the feathery sides of the TBC columns partially sinter together by surface diffusion during electron beam deposition. The columns share the same crystallographic growth axes, and possess a square cross-section of side-length d. Neighbouring columns impinge in the manner of two rough surfaces, and the diffusion-driven growth of junctions is reminiscent of diffusion bonding. In order to develop a tractable micromechanical model of the evolution of contact, the roughness of both surfaces is combined into a single wavy surface while the other surface is treated as perfectly flat. Further, it is assumed that the roughness is primarily on the length scale of the feathery arms of the TBC columns, with a wavelength λ. This is justified by the observation that roughness on a finer scale is rounded off early in the service life, as discussed by Lughi et al. [2], for example. The local roughness is idealised by the plane strain configuration shown in Fig. 3. As sintering proceeds, the contact width $2b$ increases and the combined peak-to-peak amplitude of the roughness w decreases, while the wavelength λ remains fixed. In order to reduce the number of geometrical variables in the problem, we adopt a saw-tooth profile for the roughness. The reference configuration is given in Fig. 3(a) while the geometry at a typical instant can be characterised by the geometrical parameters (u, w) as shown in Fig. 3(b). Note that the reference configuration in Fig. 3(a) is introduced for algebraic convenience only, and conceptually defines the pre-sintered state. However, sintering occurs during both deposition and service, and so the reference state is not physically realised: the TBC has already partially sintered after deposition.

The problem posed is to solve for the local evolution of surface profile as characterised by (u, w) due to the interfacial diffusion of matter from the contacts into the gaps of

peak-to-peak amplitude w. Interfacial diffusion is driven by the combined driving forces of the net reduction in interfacial energy, and the bulk elastic strain energy of the TBC as given by Eq. (4).

Straightforward geometrical arguments can be used to relate the contact width $2b$ and the inclination β to the primary unknowns (u, w). Incompressibility dictates

$$2b = \left(\frac{2u + w - w_0}{w}\right)\lambda \tag{5}$$

with

$$\tan\beta = \frac{2w^2}{(w_0 - 2u)\lambda} \tag{6}$$

and

$$\ell = \left[w^2 + \left(\frac{(w_0 - 2u)\lambda}{2w}\right)^2\right]^{1/2}. \tag{7}$$

3.2.2. The local sintering problem

It is assumed that matter diffuses along the interface from the contacts, labelled OA in Fig. 4, and deposits along the free surface AB. Fick's first law states that the interfacial flux j (in units of $\mathrm{m^2\,s^{-1}}$) is related to the gradient of chemical potential μ ($\mathrm{J\,m^{-3}}$) by

$$j = -D\frac{\partial\mu}{\partial s}, \tag{8}$$

where s is the arc length and D is the interfacial diffusivity (in units of $\mathrm{m^6\,J\,s^{-1}}$). D is temperature dependent such that

$$D = \frac{\delta\Omega}{kT} D_0 \exp(-q/kT) \tag{9}$$

in terms of a reference diffusivity D_0, atomic volume Ω, interface thickness δ, thermal activation energy q and Boltzmann constant k.

Mass conservation at an interface dictates that the normal velocity of the interface v_n is related to the flux j according to

$$v_\mathrm{n} + \frac{\partial j}{\partial s} = 0. \tag{10}$$

3.3. Geometric coupling between the local and global scales

The macroscopic sintering strain is related to the local approach u of two neighbouring columns by

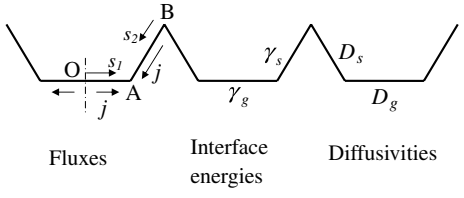

Fig. 4. Definition of fluxes, surface energies and diffusivities at the contacts.

$$\varepsilon^\mathrm{S} = \frac{u_1 - u}{d}, \tag{11}$$

where u_1 is the initial value of u after deposition. With this choice, ε^S equals zero immediately following deposition. As sintering progresses, u increases and ε^S becomes increasingly negative.

3.4. The variational problem

We are concerned with the local problem of sintering of the roughness at contacting TBC columns on a length scale λ (less than 1 μm), and can neglect the much slower diffusion over larger length scales of the order of the column diameter d (5–10 μm) and column height H (100–200 μm). Consequently, we can solve for the sintering response at any height x_3 within the thermal barrier layer. Diffusion along the x_3 direction can be neglected as the thickness of the TBC layer is much greater than the wavelength λ, and we solve for the evolution of the sintering strain $\varepsilon^\mathrm{S}(x_3, t)$ under fixed $T(x_3)$. Isothermal experiments with T independent of location x_3 and of time t are common in accelerated testing, although it is realised that engine hardware is exposed to cyclic operation. The effect of thermal cycling upon sintering is left to a subsequent study.

The variational method of Cocks et al. [6] is used to obtain $\varepsilon^\mathrm{S}(x_3, t)$, and this requires a knowledge of the total free energy per unit volume of coating G, and the dissipation Ψ arising from the local flux of matter, at any representative height x_3. An explicit relation is derived and used below for the dependence of G upon the geometric variables (u, w) at any contact. The dissipation potential Ψ is a quadratic functional of the diffusion flux, and can be re-expressed as an explicit quadratic function of the rates $(\dot{u}, \dot{w})$.

For a given geometry of TBC columns it is shown below that the rate of evolution of the microstructure is given by the set of kinematic rates $(\dot{u}, \dot{w})$ at the contacts between columns that minimise the functional

$$\Omega(\dot{u}, \dot{w}) = \dot{G}(\dot{u}, \dot{w}) + \Psi(\dot{u}, \dot{w}). \tag{12}$$

The optimal choice for $(\dot{u}, \dot{w})$ is given by the variational statement [6]

$$\delta\Omega = 0 \tag{13}$$

for arbitrary variations in $(\dot{u}, \dot{w})$. This leads to two simultaneous equations

$$\frac{\partial\dot{G}}{\partial\dot{u}} + \frac{\partial\Psi}{\partial\dot{u}} = 0 \tag{14a}$$

and

$$\frac{\partial\dot{G}}{\partial\dot{w}} + \frac{\partial\Psi}{\partial\dot{w}} = 0. \tag{14b}$$

Recall that $\dot{G}$ is linear and Ψ is quadratic in the rates $(\dot{u}, \dot{w})$. Eqs. (14) can thereby be expressed in matrix form as

$$\begin{pmatrix} \frac{\partial^2 \Psi}{\partial \dot{u}^2} & \frac{\partial^2 \Psi}{\partial \dot{u}\,\partial \dot{w}} \\ \frac{\partial^2 \Psi}{\partial \dot{u}\,\partial \dot{w}} & \frac{\partial^2 \Psi}{\partial \dot{w}^2} \end{pmatrix} \begin{pmatrix} \dot{u} \\ \dot{w} \end{pmatrix} = - \begin{pmatrix} \frac{\partial \dot{G}}{\partial \dot{u}} \\ \frac{\partial \dot{G}}{\partial \dot{w}} \end{pmatrix}. \tag{15}$$

This can be inverted algebraically to obtain $(\dot{u}, \dot{w})$ as a function of the current state (u, w). The time evolution of (u, w) follows by time integration using any convenient scheme: here, the equations are well conditioned and the forward Euler method suffices.

3.4.1. Determination of the free energy G

Consider the interfacial free energy G_λ of a slice, of thickness λ in the x_3 direction, of a single column. The column has a side length d and the slice has a projected surface area (normal to the surface of the column) of $2d\lambda$; the factor of 2 arises because the faces of the four-sided column are shared by neighbouring columns. Then, G_λ can be written in terms of the surface energy γ_S and interfacial energy at the contacts γ_G (see Fig. 4) according to

$$G_\lambda = 2d[2b\gamma_G + 2\ell\gamma_S + (\lambda - 2b)\gamma_S]. \tag{16}$$

Note that G_λ can be re-expressed as a non-linear function of (u, w) upon making use of Eqs. (5) and (7). The total free energy *per unit volume* of the TBC layer G is given by the sum of the contributions from the interfacial free energy $G_\lambda/d^2\lambda$ and the elastic strain energy density U to give

$$G = \frac{G_\lambda}{d^2\lambda} + U. \tag{17}$$

The energy density U has already been specified by Eq. (4), and the elastic strain components $\varepsilon^E_{11} = \varepsilon^E_{22}$ can be related directly to u according to Eqs. (2) and (11), at any imposed value of thermal strain ε^T. The time rate of change of free energy $\dot{G}$ is linear in $(\dot{u}, \dot{w})$ and follows directly by time differentiation of Eq. (17), giving

$$\begin{aligned} \dot{G}(\dot{u}, \dot{w}) = {} & \frac{2(\gamma_G - \gamma_S)}{dw^2}[w(2\dot{u} + \dot{w}) - (2u + w - w_0)\dot{w}] \\ & - \frac{2E}{1-\nu}\left(\varepsilon^T + \frac{u_1 - u}{d}\right)\frac{\dot{u}}{d} + \frac{2\gamma_S}{d\lambda} \\ & \times \left[\left(w^2 + \left(\frac{(w_0 - 2u)\lambda}{2w}\right)^2\right)^{-1/2} \right. \\ & \left. \times \left(2w\dot{w} - \frac{\lambda^2}{2w^3}(w_0 - 2u)(2w\dot{u} + (w_0 - 2u)\dot{w})\right)\right]. \end{aligned} \tag{18}$$

3.4.2. Determination of the dissipation potential

Next, we introduce the dissipation potential Ψ_λ per column, for a slice of thickness λ. The potential Ψ_λ is expressed in terms of the volumetric flux per unit depth j; this interfacial flux is a function of the local co-ordinate s_1 along the contact OA, and of the local co-ordinate s_2 along the contact AB, as shown in Fig. 4. Define

$$\Psi_\lambda = \frac{2d}{D_G}\int_0^b j^2(s_1)\,\mathrm{d}s_1 + \frac{2d}{D_S}\int_0^\ell j^2(s_2)\,\mathrm{d}s_2, \tag{19}$$

where (D_G, D_S) are the diffusion constants for interfacial diffusion along OA and surface diffusion along the free surface AB, respectively, as specified by Eq. (9). Now the flux $j(s_1)$ along OA is related directly to the rate of approach $\dot{u}$ of two contacting columns by the kinematic relation of Eq. (10), giving

$$j = \dot{u}s_1 \quad \text{on OA}. \tag{20}$$

Similarly, the flux $j(s_2)$ along AB is obtained from the normal velocity of the free surface v_n upon invoking Eq. (10), to give

$$\frac{\partial j(s_2)}{\partial s_2} = -v_n. \tag{21}$$

Geometry dictates that v_n can be stated in terms of $(\dot{u}, \dot{w})$ according to

$$v_n = -(\dot{u} + \dot{w})\cos\beta + \frac{s_2}{\ell}(\dot{w}\cos\beta + \dot{b}\sin\beta) \tag{22}$$

with $\dot{b}(\dot{u}, \dot{w})$ given by the rate form of Eq. (5). Integration of Eq. (21) with Eq. (22) gives

$$j = s_2(\dot{u} + \dot{w})\cos\beta - \frac{s_2^2}{2\ell}(\dot{w}\cos\beta + \dot{b}\sin\beta). \tag{23}$$

The macroscopic dissipation per unit volume of TBC Ψ is related to Ψ_λ by

$$\Psi = \frac{\Psi_\lambda}{d^2\lambda}. \tag{24}$$

An explicit expression for Ψ is obtained by integration of Eq. (19), using Eqs. (20) and (23) for the fluxes, to give

$$\begin{aligned} \Psi(\dot{u}, \dot{w}) = {} & \frac{2}{3}\frac{b^3}{d\lambda D_G}\dot{u}^2 + \frac{2\ell^3\cos^2\beta}{3d\lambda D_S}(\dot{u} + \dot{w})^2 \\ & + \frac{\ell^3}{10d\lambda D_S}\left[\dot{w}\cos\beta + \left(\frac{\lambda}{2}\left(\frac{w_0 - 2u}{w^2}\right)\dot{w} + \frac{\lambda\dot{u}}{w}\right)\sin\beta\right]^2 \\ & - \frac{\ell^3\cos\beta}{2d\lambda D_S}(\dot{u} + \dot{w})\left(\dot{w}\cos\beta \right. \\ & \left. + \frac{\lambda\sin\beta}{2w^2}(w_0 - 2u)\dot{w} + \frac{\lambda\sin\beta}{w}\dot{u}\right). \end{aligned} \tag{25}$$

3.5. Numerical solution

It is helpful to non-dimensionalise the problem in order to minimise the number of variables. All length scales are normalised by the wavelength of roughness λ, such that

$$\bar{u} = \frac{u}{\lambda}; \quad \bar{w} = \frac{w}{\lambda}; \quad \bar{b} = \frac{b}{\lambda}; \quad \bar{\ell} = \frac{\ell}{\lambda}; \quad \bar{d} = \frac{d}{\lambda}. \tag{26a}$$

The appropriate non-dimensional time scale is

$$\bar{t} = \frac{D_S\gamma_S t}{\lambda^4} \tag{26b}$$

and the non-dimensional material properties are

$$\bar{D}_G = \frac{D_G}{D_S}, \quad \bar{\gamma}_G = \frac{\gamma_G}{\gamma_S}, \quad \bar{E} = \frac{E\lambda}{(1-\nu)\gamma_S}. \tag{26c}$$

We note in passing that the non-dimensionalisation of Eqs. (26) indicates that the sintering time is sensitive to the wavelength of roughness λ. (This is well known. Recall that interfacial diffusion-controlled sintering rates scale with grain size to the power of -4.) Unless otherwise stated, we shall assume that $\bar{d} = 20$, $\bar{D}_G = 1$ and $\bar{\gamma}_G = 0.68$ [7].

3.6. Predictions

The simultaneous algebraic equation (15) are solved and time-integrated by a forward Euler scheme from an initial state of $u_1/\lambda = 0.05$ and $\bar{w} = 0.5$. Two types of behaviour are observed, depending upon the magnitude of $\bar{E}$. If $\bar{E}$ is sufficiently small, then the elastic constraint retards the rate of sintering but does not switch it off. An example is shown in Fig. 5(a), for $\bar{E} = 980$ and for vanishing thermal strain $\varepsilon^T = 0$. Full sintering occurs over a finite time scale. Then, the roughness amplitude $\bar{w}$ decreases monotonically to zero and the magnitude of the sintering strain ε^S increases to a saturated finite value with increasing time. The strain at full sintering can be deduced directly from Eqs. (5) and (11) by taking the limit $2b = \lambda$, giving a final strain of $(2u_1 - w_0)/2d = -1\%$ in this case. Note that the aspect ratio of the void β quickly establishes itself to an almost constant value as the void shrinks.

In contrast, when $\bar{E}$ is large, the build-up of elastic strain energy within the TBC layer is sufficient to switch off the later stages of sintering, and the neck size $\bar{b}$ asymptotes to a value of less than 0.5. Consequently, the asymptotic value of sintering strain does not attain the limiting value of $(2u_1 - w_0)/2d = -1\%$. An example is shown in Fig. 5(b) for the choice $\bar{E} = 1000$. Note that the early stages of the sintering responses are qualitatively similar for the choices $\bar{E} = 980$ and 1000, with the establishment of asperities of constant inclination β. However, the higher modulus leads to an arrest of the sintering process prior to full densification. The sharp nature of this transition with increasing $\bar{E}$ is evident from a plot of the final values of $\bar{b}$ and ε^S versus $\bar{E}$, as shown in Fig. 6 for selected values of thermal strain ε^T. The build-up of elastic strain energy is sufficient to switch off sintering for $\bar{E}$ above a threshold value. It is concluded from Fig. 6 that the extent of inter-columnar sintering is minimised by minimising the thermal mismatch strain ε^T and maximising the in-plane elastic modulus of the TBC layer.

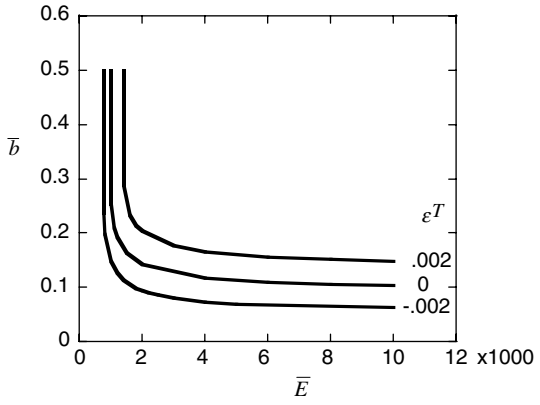

Fig. 6. Effect of in-plane modulus upon the final neck size, for selected values of thermal strain ε^T.

Numerical experimentation revealed that the overall sintering response is only mildly sensitive to the initial choice of neck size $\bar{b}$. The two thermodynamic driving forces $\partial\dot{G}/\partial\dot{u}$ and $\partial\dot{G}/\partial\dot{w}$ can be interpreted as follows. The force $\partial\dot{G}/\partial\dot{u}$ drives the flattening of the asperities and leads to the sintering strain in a direct manner. In contrast, the force $\partial\dot{G}/\partial\dot{w}$ dictates the change in shape of the gaps between asperities, and in particular the angle β. It has been observed from numerical simulations over a wide range of parameters that β quickly settles down to a constant value, implying that $\partial\dot{G}/\partial\dot{w}$ is almost zero. This allows for a simpler description of the evolving microstructure. By formally setting $\partial\dot{G}/\partial\dot{w}$ to zero, the inclination β follows from Eq. (18) as

$$4\cos\beta = (\bar{\gamma}_G - 1) + \sqrt{(\bar{\gamma}_G - 1)^2 + 8}. \tag{27}$$

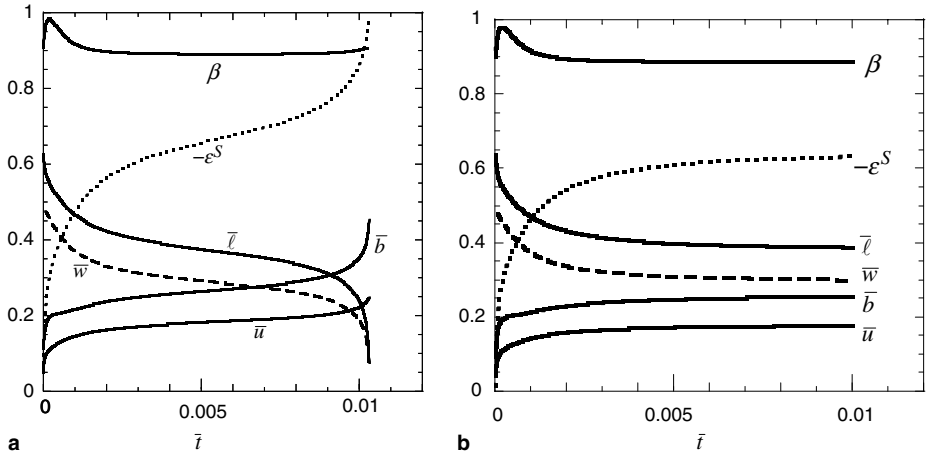

Fig. 5. Evolution of contact geometry and sintering strain (%) for the choice (a) $\bar{E} = 980$, and (b) $\bar{E} = 1000$. The inclination β is in radians.

For the choice $\bar{\gamma}_G = 0.68$ this gives $\beta = 0.887$, which is consistent with the steady-state value shown in Figs. 5(a) and (b). With β held fixed, the sintering problem reduces to a single degree of freedom problem, with u as the primary unknown. The algebra of this *reduced model* is omitted here for the sake of brevity, but we note in passing that an implicit algebraic expression can be obtained for the final value of contact size $\bar{b}$ by setting $\partial\dot{G}/\partial\dot{u}$ equal to zero. Incomplete sintering occurs for values of

$$\bar{E} \geqslant \frac{3\sqrt{3}(1-\bar{\gamma}_G+1/\cos\beta)}{2(\bar{d}\tan\beta)^{\frac{3}{2}}\left(\frac{w_0}{2d}-\frac{u_1}{d}-\varepsilon^T\right)^{\frac{3}{2}}}. \tag{28a}$$

For values of $\bar{E}$ which satisfy this inequality the final contact size can be obtained from the implicit expression

$$2(\bar{\gamma}_G-1-1/\cos\beta) = \bar{E}\tan\beta(1-2\bar{b}) \times\left(\varepsilon^T+\frac{u_1}{d}-\frac{w_0}{2d}+\frac{1}{4\bar{d}}(1-2\bar{b})^2\tan\beta\right). \tag{28b}$$

The predictions of (28a) and (28b) are in excellent agreement with the results plotted in Fig. 6.

4. Problem B: sintering within a mud-cracked layer

Sintering between the columns leads to a build-up of in-plane tension. If the magnitude of this tension is sufficiently high it may switch off the sintering process or it may lead to inter-columnar mud-cracking. A brief discussion of the prediction of mud-cracking is given in Section 5; at this point, we assume that a fully developed mud-cracking pattern has been developed, with the TBC columns grouped into a hexagonal arrangement of clusters, as shown in Fig. 2(b). For computational convenience, we idealise each cluster as a circular cylindrical column of radius R and height H, perfectly bonded to the underlying TGO, see Fig. 7. The side and top of each cluster is traction-free, thereby reducing the level of in-plane tensile stress to less than the uncracked value as specified by Eqs. (2) and (3). The drop in stored elastic strain energy within the cluster leads to a drop in the level of elastic constraint against sintering. Consequently, inter-columnar sintering is accelerated by the occurrence of the mud-cracking.

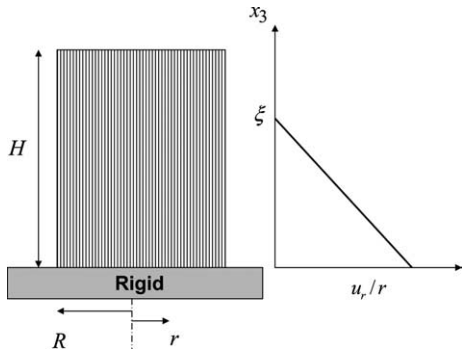

Fig. 7. A single cluster of columns of height H and radius R, with the assumed radial displacement distribution throughout the cluster.

We limit attention to the isothermal case such that the thermal strain is uniform within the cracked TBC. For simplicity, we shall assume that the sintering strain ε^S is uniform throughout the TBC but can evolve with time. A kinematically admissible elastic strain field is adopted for the deformation of the columns within the representative cluster, and this allows for an estimation of the stored elastic strain energy. (Finite element methods are required in order to predict a non-uniform distribution of ε^S and non-uniform elastic strain field.) The intent here is to provide an analytical framework in order to assess the significance of mud-cracking to first order.

The local sintering problem between columns is the same as that for the uncracked TBC, and can be described in terms of the local internal state variables $(\dot{u},\dot{w})$. Sintering is again driven by local interfacial energy, and dissipation is again due to interfacial diffusion. However, the analysis now proceeds at the level of a single cluster of columns.

4.1. Estimation of the stored elastic strain energy within a cluster of columns

The elastic strain energy within a circular, cylindrical cluster U_C is estimated by assuming that the cluster is given a uniform in-plane, stress-free transformation strain of $(\varepsilon^T+\varepsilon^S)$, with full constraint against radial motion imposed along the bottom surface, $x_3 = 0$. An Eshelby-type cut-and-paste procedure implies that the elastic component of radial displacement at the base of the column, $x_3 = 0$, is

$$u_r = -(\varepsilon^T+\varepsilon^S)r, \tag{29}$$

where r is the radial co-ordinate from the centreline of the cluster. In order to estimate the stored elastic strain energy in the cluster it is envisaged that elastic straining occurs within a slice of thickness ξ within the TBC coating. Assume a simple, kinematically admissible field which satisfies this boundary condition. Here, we take

$$u_r(r,x_3) = -(\varepsilon^T+\varepsilon^S)\left(1-\frac{x_3}{\xi}\right)r \tag{30a}$$

for $0 \leqslant x_3 \leqslant \xi$, and

$$u_r(r,x_3) = 0 \tag{30b}$$

for $\xi < x_3 \leqslant H$ as shown in Fig. 7. A rational method for determining ξ is to select its value such that the elastic strain energy of the cluster U_C is minimised. Assuming elastic incompressibility, we find that the elastic displacement in the x_3 direction is

$$u_3 = (\varepsilon^T+\varepsilon^S)\left(2x_3-\frac{x_3^2}{\xi}\right), \quad 0 \leqslant x_3 \leqslant \xi \tag{31a}$$

and

$$u_3 = (\varepsilon^T+\varepsilon^S)\xi, \quad \xi < x_3 \leqslant H. \tag{31b}$$

Consequently, the elastic strain energy of the cluster U_C is

$$U_C = \frac{2\pi}{3}ER^2(\varepsilon^T+\varepsilon^S)^2\left(\xi+\frac{R^2}{8\xi}\right). \tag{32}$$

The optimal value of ξ is obtained by minimising U_C with respect to ξ, and this suggests that

$$\xi = \frac{R}{2\sqrt{2}} \tag{33}$$

giving

$$U_C = \frac{\sqrt{2}}{3}\pi E R^3(\varepsilon^T + \varepsilon^S)^2. \tag{34}$$

Eq. (34) is valid provided H exceeds $R/2\sqrt{2}$. If H is less than $R/2\sqrt{2}$, an appropriate choice for $u_r(r, x_3)$ is

$$u_r(r, x_3) = -(\varepsilon^T + \varepsilon^S)\left(1 - 2\sqrt{2}\frac{x_3}{R}\right)r \tag{35}$$

for $0 \leqslant x_3 \leqslant H$. The strain energy of the cluster U_C is then

$$U_C = \frac{2}{3}\pi E R^2\left[\frac{R}{2\sqrt{2}}\left\{1 - \left(1 - 2\sqrt{2}\frac{H}{R}\right)^3\right\} + H\right](\varepsilon^T + \varepsilon^S)^2. \tag{36}$$

The stored elastic strain energy per unit volume of TBC is given by

$$U = \frac{U_C}{\pi R^2 H} \tag{37}$$

with U_C specified by Eq. (34) for the case $H \geqslant R/2\sqrt{2}$ and by Eq. (36) for $H < R/2\sqrt{2}$. In comparison, the strain energy per unit volume in the uncracked incompressible film ($v = 0.5$) follows from Eq. (4) as

$$U = 2E(\varepsilon^T + \varepsilon^S)^2. \tag{38}$$

It is evident that the effect of the mud-cracking is to reduce the level of stored elastic strain energy compared with that of the uncracked film, problem A. The variational principle is applied as before, with the total free energy *per unit volume* of the TBC layer G given by Eq. (17), and the macroscopic dissipation per unit volume of TBC Ψ specified by Eq. (25).

4.2. Predictions of sintering within mud-cracked columns

The solution procedure proceeds as before for the uncracked TBC layer, in problem A. The simultaneous algebraic equation (15) is solved and time-integrated by a forward Euler scheme from an initial state of $u_1/\lambda = 0.05$ and $\bar{w} = 0.5$. The solution now depends upon the additional non-dimensional group $\bar{H} = H/R$.

The effect of mud-cracking upon the sintering rate is illustrated by comparing the prediction for a mud-cracked layer with $\bar{H} = 1$ in Fig. 8 with the equivalent uncracked layer taken from Fig. 5(b), both for the choice of $\bar{E} = 1000$ and $\varepsilon^T = 0$. The in-plane modulus is sufficiently high for sintering to be switched off in the uncracked layer, while the reduced constraint of the mud-cracked layer leads to full sintering between columns. The sensitivity of the final size of neck $\bar{b}$ to the in-plane modulus is shown in Fig. 9 for selected values of aspect ratio $\bar{H} = H/R$ of mud-cracked columns, and for the choice $\varepsilon^T = -0.002$. Full sintering, such that the final value of $\bar{b}$ equals 0.5, occurs at low value of $\bar{E}$ and is encouraged by high values of $\bar{H}$ due to the reduction in elastic constraint.

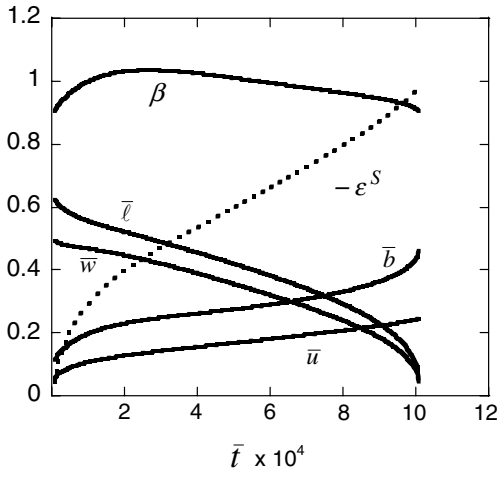

Fig. 8. Evolution of contact geometry and sintering strain (%) for $\bar{E} = 1000$, $\bar{H} = 1$ and $\varepsilon^T = 0$. The inclination β is in radians.

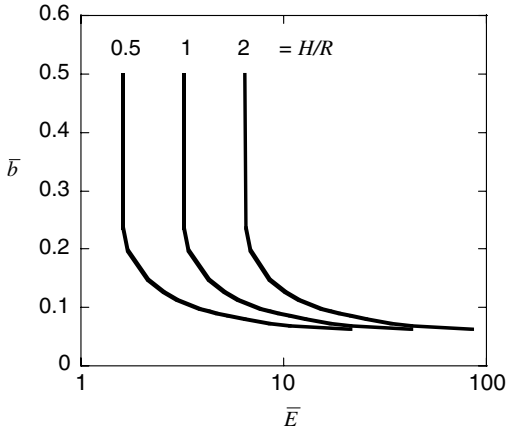

Fig. 9. Final neck size $\bar{b}$ versus modulus ratio $\bar{E}$, for selected values of aspect ratio $\bar{H} = H/R$ of mud-cracked columns, and $\varepsilon^T = -0.002$.

5. Discussion

It is likely that mud-cracking of the TBC layer occurs at cool-down during cyclic operation of a gas turbine engine. However, the evolution of the density of mud-cracks with operation is unknown. It is argued here that mud-cracking is a consequence of the build-up of in-plane tensile stress within the TBC layer by the sintering of the TBC columns. Estimates are now given for the combined level of sintering strain ε^S and thermal mismatch strain ε^T to induce mud-cracking.

5.1. Threshold condition for mud-cracking

The problem of channelling of a crack within a thin bonded film in residual tension has been addressed by Beuth [8]. He considered the threshold level of in-plane

tensile stress required for a crack to channel across the film in steady state. Here, we limit his predictions to the case where the film and substrate share identical elastic constants, and the crack channels to the bottom of the film of thickness H, and of mode I toughness G_{IC}. The threshold level of stress σ_{th} is

$$\sigma_{th} = \frac{1}{1.1215}\sqrt{\frac{2}{\pi}}\left(\frac{EG_{IC}}{(1-\nu^2)H}\right)^{1/2}. \tag{39}$$

Now the in-plane stress level σ is related to the sintering strain ε^S and thermal mismatch strain ε^T according to Eqs. (2) and (3), such that

$$\sigma = -\frac{E}{(1-\nu)}(\varepsilon^T + \varepsilon^S). \tag{40}$$

Upon combining with Eq. (39), we obtain the threshold strain level for channelling

$$(\varepsilon^T + \varepsilon^S)_{th} = -\frac{1}{1.1215}\left(\frac{2(1-\nu)}{\pi(1+\nu)}\frac{G_{IC}}{EH}\right)^{1/2}. \tag{41}$$

It is clear from Eq. (41) that mud-cracking is encouraged by a low value of toughness between columns, and by a high in-plane modulus and thick TBC layer. It is reasonable to assume that the effective toughness G_{IC} between columns scales with the area fraction $2\bar{b}$ of sintered necks between columns, and with the toughness of the solid G_S according to

$$G_{IC} = 2\bar{b}G_S. \tag{42}$$

As inter-columnar sintering proceeds the area fraction $2\bar{b}$ increases, while the sintering strain ε^S becomes more negative. In the sintering evolution calculations presented above, the increase in effective modulus E with increasing neck size $2\bar{b}$ is neglected. (More refined calculations are required in order to determine the relationship between E and $2\bar{b}$.) Substitution of Eq. (42) into Eq. (41) provides a combined parameter I for the onset of channelling

$$I > I_{th}, \tag{43}$$

where

$$I \equiv -\varepsilon^S - \frac{1}{1.1215}\left(\frac{2(1-\nu)}{\pi(1+\nu)}\frac{2\bar{b}G_S}{EH}\right)^{1/2} \tag{44}$$

and

$$I_{th} = \varepsilon^T \tag{45}$$

I increases as sintering progresses and may or may not attain the threshold condition for channelling.

5.2. Prediction of evolution of density of mud-cracks

Now consider the case where the sintering strain is sufficiently large and negative for mud-cracking to initiate during the service life of the TBC coating. An estimate for the evolution of mud-cracking density can be obtained by assuming that the rate of decrease in strain energy with additional mud-cracking equals the rate of increase of surface area times the inter-columnar toughness.

Assume that the TBC layer is in a mud-cracked state, and comprises clusters of average radius R. Then, the ratio of surface area of cracks per unit volume of TBC layer is

$$f = 1/R. \tag{46}$$

The initial stored elastic energy within the uncracked TBC layer is

$$U_0 \equiv \frac{E}{1-\nu}(\varepsilon^T + \varepsilon^S)^2 \tag{47}$$

via Eqs. (2) and (4), and the presence of mud-cracking decreases this value to

$$U = \frac{\sqrt{2}}{3}E\frac{R}{H}(\varepsilon^T + \varepsilon^S)^2 \tag{48}$$

according to Eq. (34), provided $H/R \geqslant 1/2\sqrt{2}$. If H/R is less than $1/2\sqrt{2}$, the strain energy density follows from Eq. (36) as

$$U = \frac{2}{3}E\left[\frac{1}{2\sqrt{2}}\frac{R}{H}\left\{1-\left(1-2\sqrt{2}\frac{H}{R}\right)^3\right\}+1\right](\varepsilon^T + \varepsilon^S)^2. \tag{49}$$

Now we equate $\partial(U_0 - U)/\partial f$ to G_{IC} to obtain from Eqs. (47) and (48)

$$\varepsilon^T + \varepsilon^S = -\left(\frac{3}{\sqrt{2}}\frac{G_{IC}}{EH}\right)^{1/2}\frac{H}{R} \tag{50}$$

provided $H/R \geqslant 1/2\sqrt{2}$. For $H/R < 1/2\sqrt{2}$, Eqs. (47) and (49) give

$$\varepsilon^T + \varepsilon^S = -\left(\frac{3}{\sqrt{2}}\frac{G_{IC}}{EH}\right)^{1/2}\frac{1}{2(3-4\sqrt{2}H/R)^{1/2}}. \tag{51}$$

Eqs. (50) and (51) give the evolution of mud-cracking density as parameterised by H/R with increasing degree of inter-columnar sintering $-\varepsilon^S$. The dependence of H/R upon $(\varepsilon^T + \varepsilon^S)$ is plotted in Fig. 10, including the

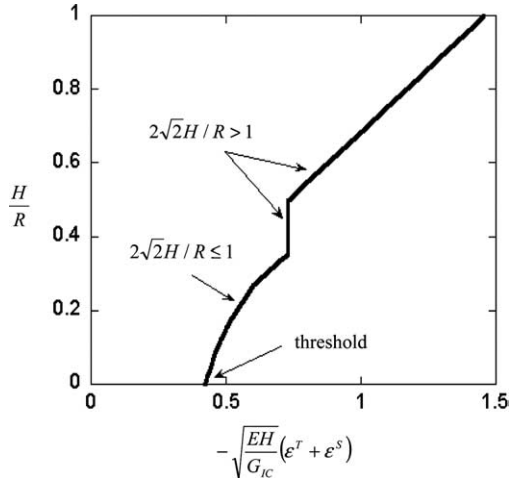

Fig. 10. The evolution of mud-cracking density with sintering strain.

threshold value of $(\varepsilon^{T} + \varepsilon^{S})$ as given by Eq. (41), for the case of an incompressible solid $\nu = 0.5$. The figure is interpreted as follows. At sufficiently small values of $-(\varepsilon^{T} + \varepsilon^{S})$ below the threshold value, no mud-cracking is anticipated. Once the threshold value has been attained, as specified by Eq. (41), mud-cracking initiates, and in the dilute case of non-interacting mud-cracks (small H/R), the density of mud-cracks increases sharply with increasing $-(\varepsilon^{T} + \varepsilon^{S})$. Subsequently, the density of mud-cracks as parameterised by H/R increases linearly with $-(\varepsilon^{T} + \varepsilon^{S})$. And now a word of caution. The analysis so far is based upon an approximate formula for the strain energy density $U(H/R)$. More sophisticated calculations are desirable to improve upon the numerical accuracy of the prediction given in Fig. 10. However, we expect the qualitative trends to be preserved, and in particular the increase in mud-cracking density with the progression of inter-columnar sintering.

6. Concluding remarks

The above treatment is not meant to capture every nuance of TBC sintering behaviour, but rather to capture the essential micromechanics of TBC sintering and to explore its coupling with the phenomenon of mud-cracking. The build-up of in-plane tensile stress with inter-columnar sintering can trigger mud-cracking, and in turn the mud-cracking can partially relieve this stress and promote subsequent sintering. As the columns within each cluster continue to sinter, the opening of each mud-crack increases, and this may have consequences upon the overall integrity of the TBC system. The cracks may allow chemical ingress to the TGO and bond coat, and may lead to spallation at the base of the TBC layer. These remaining problems are suggested as topics for future research.

Acknowledgements

The research was supported by a programme of international collaboration between the National Science Foundation (DMR-0099695) and the European Commission (GRD2-200-30211).

References

[1] Evans AG, Mumm DR, Hutchinson JW, Meir GH, Pettit FS. Prog Mater Sci 2001;46:505.
[2] Lughi V, Tolpygo K, Clarke DR. Mater Sci Eng A 2004;368:212.
[3] Azzopardi A, Mevrel R, Saint-Ramond B, Olson E, Stiller K. Surf Coat Technol 2004;177–178:131.
[4] Wellman RG, Nicholls JR. Surf Coat Technol 2004;177:80.
[5] Clarke DR, Levi CG. Annu Rev Mater Res 2003;33:383.
[6] Cocks ACF, Gill SPA, Pan J. In: van der Giessen E, Wu TY, editors. Advances in applied mechanics, vol. 36. New York (NY): Academic Press; 1999. p. 82.
[7] Swinkels FB, Ashby MF. Acta Metall 1981;29:259.
[8] Beuth JL. Int J Solid Struct 1992;29:1657.